Journal of Power Sources 196 (2011) 4088–4094

Contents lists available at ScienceDirect

Journal of Power Sources

journal homepage: www.elsevier.com/locate/jpowsour

Synthesis of mesoporous polythiophene/MnO_2 nanocomposite and its enhanced pseudocapacitive properties

Qing Lu*, Yikai Zhou

MOE Key Lab of Environment and Health, School of Public Health, Tongji Medical College, Huazhong University of Science and Technology, Wuhan 430030, PR China

ARTICLE INFO

Article history:
Received 20 September 2010
Accepted 16 December 2010
Available online 24 December 2010

Keywords:
Manganese oxide
Polythiophene
Mesoporous nanocomposite
Supercapacitor

ABSTRACT

Mesoporous nanocomposite of polythiophene and MnO_2 has been synthesized by a modified interfacial method, aiming to develop electrode materials for supercapactitors with an enhanced cycle performance and high-rate capability. The N_2 adsorption/desorption isotherm test of the prepared hybrid indicates a high surface area and a typical mesoporous feature. A uniform hierarchical microstructure with submicron-spheres assembled from ultrathin nanosheet with diameters less than 10 nm has been confirmed by field-emission scanning electron microscopy and transmission electron microscopy. The employed interfacial synthesis is found to be advantageous to retard the overgrowth of nuclei. The retention of 97.3% of its initial capacitance after 1000 cycles at a charge/discharge rate of 2 A g^{-1} indicates excellent cycle performance of the nanocomposite electrode. At a high-rate charge/discharge process of 10 A g^{-1}, the nanocomposite electrode retained 76.6% of its capacitance at 1 A g^{-1}, suggesting good high-power capability. The important roles of polythiophene in the as-prepared nanocomposite are highlighted in terms of their functions on enhancing the electrical conductivity and constraining the dissolution of manganese oxides during charge–discharge cycles.

1. Introduction

Supercapacitors (SCs) that feature high power density and long cycle life have raised enormous attractions owing to their promising applications as supplementary power sources for batteries and fuel cells in electric vehicles and digital devices [1,2]. At present, ruthenium oxide hydrates are acknowledged as the highly active electrode materials for SCs due to their high specific capacitance, good high-rate performance [3]. However, the high cost and toxicity of ruthenium-based raw materials imposed constraint on their large-scale applications. Among different types of alternative candidates ranging from carbons, transition metal oxides to polymers, manganese oxides are of lower cost and less environmental concerns compared to RuO_2 [4–8]. However, the specific capacitance and rate capability of manganese oxide-based materials are yet inferior to that of ruthenium dioxide-based materials. It is known that the pseudo-capacitance of manganese oxides is derived from the surface adsorption/desorption of electrolyte cations [8] and cations' reversible intercalation/de-intercalation into oxides' lattices [9,10]. Thus, nanostructured manganese oxides exhibit enhanced kinetics and activity derived from their larger surface areas and shorter solid-state transport length, compared with their bulky counterparts [11,12]. There still remains a challenge to controllable synthesis of ultrathin manganese oxides with diameters less than 10 nm although many wet chemical routes have been developed to prepare different shapes of nanostructured manganese oxides [13–15]. The forenamed challenge can be ascribed to the extremely high surface energy of ultrathin nanoparticles. The tiny nanoparticles with high surface energy tend to agglomerate during the course of synthesis and electrode fabrication [16]. The porosity and pore-size distribution also play important roles in determining the diffusion efficiency of electrolyte and ions, and thus determining the electrode effective surface area which is accessible to electrolyte and ions during the charge/discharge process [17–19]. Therefore, it will be of importance but a challenge to facilely prepare nanostructured manganese oxides with defined porosity and pore-size distribution.

For fulfilling good high-power capabilities of SCs, electrodes should possess good electrical conductivity to facilitate rapid electron transfer. However, the relatively low electrical conductivities of pristine manganese oxides, to a great extent, limit their high-rate performances [20,21]. The intrinsic manganese oxides are generally decorated with conducting agents, such as carbons and conducting polymers, in order to enhance their electrical conductivities [22–29]. In particular, good electrical conductivities and fast electrochemical doping/undoping redox kinetics of conducting polymers make them potential alternative electrode materials for high-rate SCs [30]. However, conducting polymers potentially fall victim to their poor mechanical stability and

* Corresponding author. Tel.: +86 27 83692333; fax: +86 27 83657765.
E-mail address: qiweiliao@gmail.com (Q. Lu).

0378-7753/$ – see front matter © 2010 Elsevier B.V. All rights reserved.
doi:10.1016/j.jpowsour.2010.12.059

narrow operating electrochemical windows. These demerits of conducting polymers restrain their practical applications in SCs. A general strategy to overcome the above drawbacks is to introduce conducting polymers into the matrix of other active electrode materials [22,24,26,27,29,31–36]. The corresponding composites, such as manganese oxide/conducting polymer and carbon nanotube/conducting polymer, are expected to convey enhanced electrochemical properties if each component can retain its merits and both individuals can compensate their shortcomings synergistically. However, not all attempts involving the composite systems, achieved successes [37]. It thus prompts a need to understand the synergic effects of composite in depth. Moreover, some previous studies have just focused on controllable formation of nanostructured oxides and conducting agents separately [38], rather than combining both together [16,24,39]. And some synthesis routes required expensive templates and tedious post-treatments [24]. Challenges still exist in facile synthesis and fundamental understanding of exact function of each component, although researches on manganese oxide/conducting polymer composite for advanced SC materials have emerged [22,24–27,29,33–37].

Herein, we report a facile one-pot synthesis of polythiophene/MnO_2 (PTh/MnO_2) nanocomposite with submicron-sphere/nanosheet hierarchical structures via a modified inorganic/organic interfacial route [34,35,40]. The synthesis route did not involve any expensive templates, additional structure directing agents and complex precursors. The microstructure as well as electrochemical properties of the prepared composite was thoroughly investigated. The enhanced electrochemical properties of the resulting products were discussed in terms of their microstructure and the synergic effects of both components.

2. Experimental

All chemicals are of analytical grade from *Aldrich*. In a typical interfacial synthesis, thiophene (2 ml) was dissolved in an organic phase consisting of 100 ml dichloromethane (CH_2Cl_2). Potassium permanganate (0.1 g, $KMnO_4$) was dissolved in 100 ml deionised water. And several drops of diluted hydrochloride acid (HCl) were added to the aqueous $KMnO_4$ solution to adjust the pH value to 2. Then the aqueous solution was pipetted to the organic solution drop by drop. A static organic/inorganic interface was then formed. The reaction bath was then kept in a refrigerator under a controlled temperature of 4 °C. The chemical oxidative polymerization of thiophene and the reduction of MnO_4^- to manganese oxides occurred at the interface concurrently. After 1 h reaction, dark purplish-brown powder was collected by centrifugation from the upper aqueous suspensions and then washed with deionised water for 3 times and ethanol for once before room temperature vacuum drying. For comparison, the co-precipitation synthesis was also carried out with the same parameters as those in interfacial route except for the absence of dichloromethane.

Crystallographic information of all as-prepared samples was investigated by X-ray powder diffraction (XRD; Shimadzu XRD-6000, Cu Kα, λ = 1.5406 Å) at a scanning rate of 2 °C min^{-1}. Elementary test was carried out by CHNS-O Analyser (Flash EA, 1112 Series, Thermo Electron Corporation). Thermal behaviors of samples were examined by thermogravimetric analysis (TGA, Shimadzu DTG-60) from room temperature up to 600 °C at a heating rate of 5 °C min^{-1} in air. Bonding properties of samples were characterized with Fourier transform infrared spectroscopy (FTIR, Shimadzu FTIR-8700) using a standard potassium bromide (KBr) pellet technique. Morphologies of samples were examined with field-emission scanning electron microscopy (FESEM; Hitachi, S-4300) and transmission electron microscopy (TEM, JEOL 3010, 200 kV). Elemental compositions of prepared samples were also measured with energy dispersive spectroscopy (EDS) microanalysis attached to FESEM. The Brunauer–Emmett–Teller (BET) surface area was determined by N_2 adsorption/desorption isotherm (Micromeritics Tristar 3020). The pore-size distribution was calculated using adsorption curve by the Barrett–Joyner–Halenda (BJH) method.

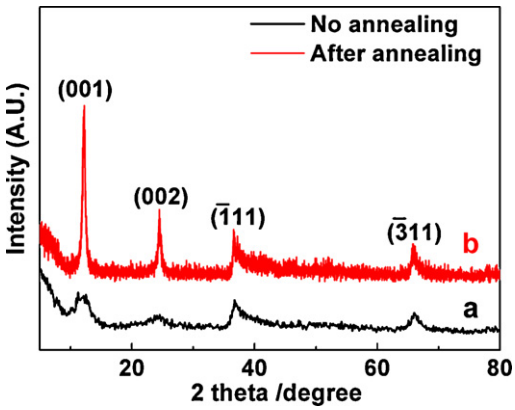

Fig. 1. Powder XRD patterns of the prepared PTh/MnO_2 nanocomposite before (a) and after (b) annealing at 400 °C for 1 h.

For electrochemical tests (Solartron SI1287), the as-synthesized powder, functioning as active material (80 wt%), was mixed with a binder (polyvinylidene difluoride, PVDF, 10 wt%) and acetylene black (10 wt%) to form a uniform slurry. The slurry was then press-coated on a 1 cm × 1 cm porous nickel meshes to make the working electrode. A balance (AND GR-202) with an accuracy of 0.01 mg was employed to confirm the mass of the active material. The typical loading of the active electrode material is 1.2–1.5 mg cm^{-2}. Electrochemical experiments were carried out in a one-compartment, three-electrode electrochemical bath containing 1.0 M sodium sulfate aqueous solution as the electrolyte, a platinum foil (2 cm × 2 cm) as the counter electrode and an Ag/AgCl reference electrode. The specific capacitance and the cycle performance of electrodes were determined from cyclic voltammograms (CV) and galvanostatic charge/discharge cycling plots. The electrochemical impedance spectroscopy (EIS) was also investigated at the open-circuit potential in the frequency range of 10^5–0.1 Hz with an amplitude of 5 mV (Solartron SI1260 impedance analyzer). The microstructure and the electrochemical properties of the prepared nanocomposite after annealing at 400 °C for 1 h were also studied.

The specific capacitance, C, can be calculated from the following equation:

$$C = \frac{Q}{m\Delta V}\ [\mathrm{F\,g^{-1}}],$$

where Q is the discharged charge which is integrated from the discharge segment of cyclic voltammograms and galvanostatic charge/discharge cycling plots, m is the mass of the active material, ΔV is the potential window.

3. Results and discussion

The XRD pattern of the as-prepared products is shown in Fig. 1a. The pattern can be indexed to the layered birnessite-type MnO_2 (JCPDS No. 80-1098, monoclinic, $C2/m$, a = 5.15 Å, b = 2.84 Å, c = 7.17 Å). The increased relative intensity of the peak located at 37.02° may be related to the scattering from polymers. The relative low-intensity and broad peaks displayed in the XRD pattern imply the low crystalline state of the sample and the existence of amorphous polymers. Birnessite-type MnO_2 has a 2-dimensional lamellar structure with an interlayer gap of 0.73 nm [41]. The relative large interlayer gap is suitable for insertion/extraction of

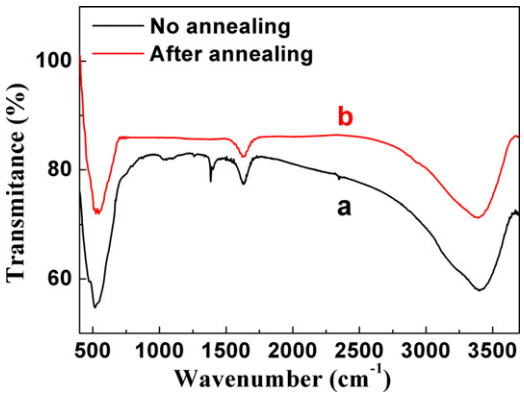

Fig. 2. FTIR spectra of the prepared PTh/MnO_2 nanocomposite before (a) and after (b) annealing at 400 °C for 1 h.

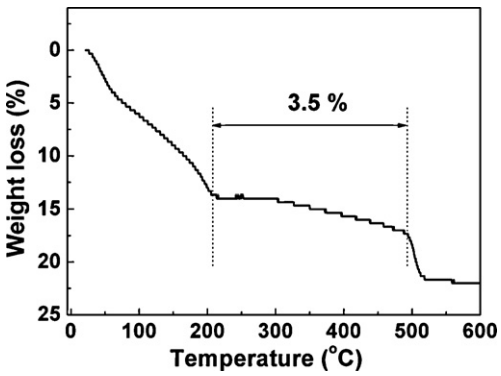

Fig. 3. TGA curve of the prepared PTh/MnO_2 nanocomposite.

alkali cations or crystal water molecules within the oxides' lattices [41,42]. Some cations and crystal water molecules can be introduced into the interlayer gap from the precursors during the synthesis process. The corresponding EDS spectrum (not shown) revealed the presence of potassium element with a K/Mn atomic ratio of 2.5%. The existence of polymer in the as-prepared product is then confirmed by FTIR, as shown in Fig. 2a. The bands from 500 to 600 cm^{-1} can be assigned to Mn–O stretching vibrations. The characteristic band at 3390 cm^{-1} is attributed to the O–H stretching

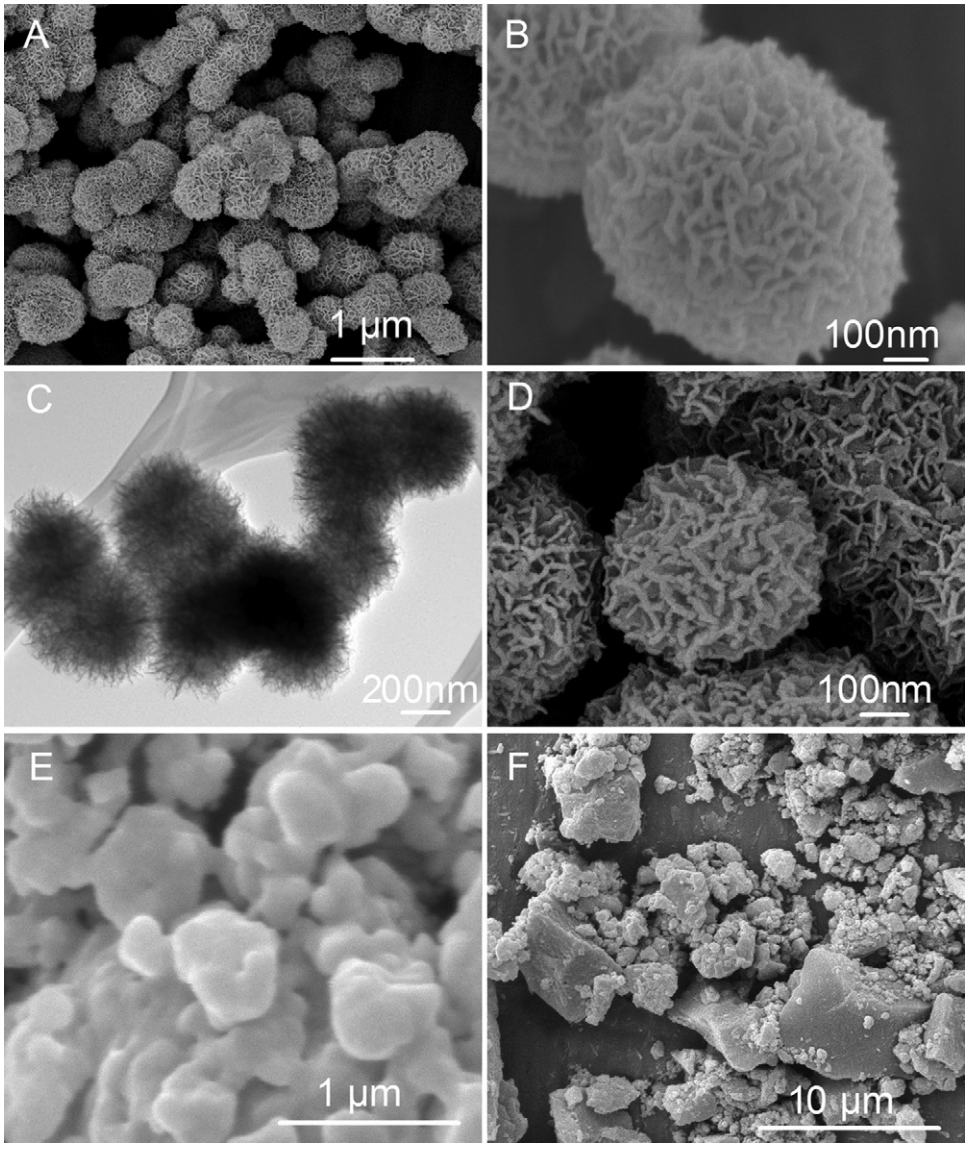

Fig. 4. Typical FESEM (A, B and D) and TEM (C) images of the prepared PTh/MnO_2 nanocomposite before (A, B and C) and after (D) annealing at 400 °C for 1 h. (E) and (F) show the typical FESEM images of the sample prepared by a co-precipitation route.

vibration. While the band at 1662 cm^{-1} is normally ascribed to the O-H bending vibration from crystal or adsorbed water molecules [40]. Vibrations between 950 cm^{-1} and 1450 cm^{-1} originate from stretching or bending bands of PTh [43,44], suggesting the presence of PTh in the sample. The elemental analysis showed that the mass content of sulfur was 1.48 wt% in the sample, which indicated that the mass content of PTh was 3.79 wt%. The mass content of PTh was also characterized by TGA measurement, following a recent reference [40]. The TGA curve of the prepared powder is illustrated in Fig. 3. The weight loss from room temperature to 200 °C can be attributed to the dehydrating of physically adsorbed and chemically bonded hydrates. The weight loss between 200 °C and 490 °C is assigned to the pyrolysis of polymers [40]. And the weight loss between 490 °C and 550 °C is derived from the self-decomposition from MnO_2 to Mn_2O_3 [45]. The weight fraction of PTh in the as-prepared composite is about 3.5 wt% based on the TGA result.

The interfacial synthesis followed by heat-treatments can be a potential method to produce intrinsic manganese oxides since polymers can be eliminated by simple heat-treatments at relatively low temperatures. The synthesized composite was heat-treated in air at 400 °C for 1 h with a heating ramp of 5 °C min^{-1} to prepare pristine manganese oxides. The XRD pattern of the sample after annealing is shown in Fig. 1b. The pattern is well-indexed to birnessite-type MnO_2. The anomalous enhanced intensity of the peak located at 37.02° becomes normal, indicating the elimination of polymers. The elimination of PTh after annealing is also confirmed by corresponding FTIR spectrum demonstrated in Fig. 2b. It conveys that all vibrations ascribed to PTh totally disappear after heat-treatments.

The FESEM images of the as-synthesized composite are shown in Fig. 4A and B. The panoramic morphology, given in Fig. 4A, indicates that the sample is composed of uniform submicron-spheres with diameters between 500 and 800 nm. Also, the high-magnification FESEM image presented in Fig. 4B clearly illustrates that the submicron-spheres consist of radial nanosheets with a thickness less than 10 nm. The submicron-sphere/nanosheet hierarchical microstructure of the synthesized composite is also verified by the corresponding TEM image displayed in Fig. 4C. The BET surface area and pore-size distribution of the generated composite were characterized by N_2 adsorption/desorption isotherm, as shown in Fig. 5. A typical type IV isotherm with a hysteresis loop of type H3 appears in the N_2 adsorption/desorption isotherm, as displayed in Fig. 5A. This type of isotherm suggests the synthesized composite has a disordered mesoporous structure, in which the mesopores arise from the packing of ultrathin nanosheets. The obtained pore-size distribution is narrow and centred around the diameter of 4 nm, as depicted in Fig. 5B. The prepared nanocomposite with well-defined nanoporous matrix is beneficial to decrease ion transfer barrier since the nanoscale pores can facilitate the penetration of electrolyte and ions through bulky electrodes. And the self-assembled ultrathin nanosheets give a high BET surface area of 110 $m^2 g^{-1}$. The morphology of annealed sample was also examined. The FESEM image of the as-obtained nanocomposite after annealing at 400 °C for 1 h is displayed in Fig. 4D. It is obvious that, after annealing, the submicron-sphere/nanosheet hierarchical microstructure is largely retained. No agglomeration of particles can be found. And the diameter of the nanosheets still remains less than 10 nm. Slightly broken spheres are shown and can be explained by the influence of thermal-induced strain. Nanomaterials generally possess inferior stability due to their high surface energy [12]. The retention of morphology and crystal phase of the prepared nanocomposite even after heat-treatments at 400 °C for 1 h indicates the good stability of the sample.

A recent literature reported the interfacial synthesis of nanocomposite of polyaniline and MnO_2, whereas the synthesized nanocomposite displayed irregular microstructure [40]. The

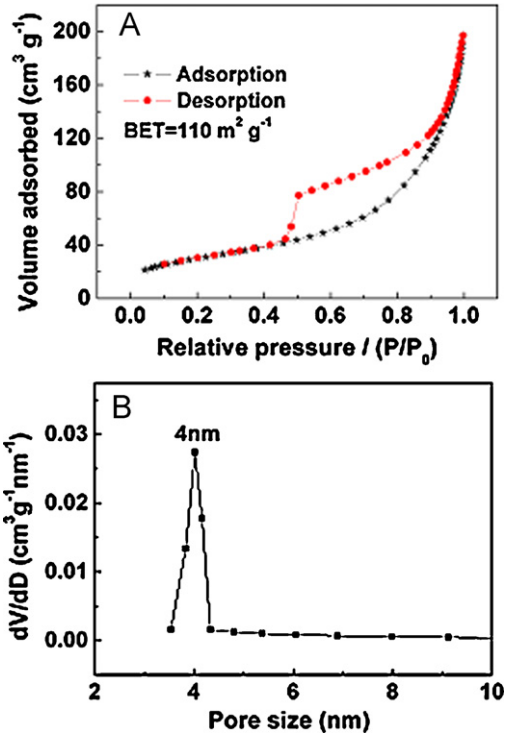

Fig. 5. N_2 adsorption/desorption isotherm (A) and pore-size distribution (B) of the prepared PTh/MnO_2 nanocomposite.

difference in morphologies may be attributed to the difference in the monomer, pH value and organic phase. It indicates the importance of tuning the synthesis parameters to engineering the product's microstructure. The growth mechanism of PTh/MnO_2 submicron-sphere/nanosheet hierarchical structure can be briefly rationalized as follows. At the beginning, the redox reaction occurs at the interface to form stoichiometric MnO_2 and radical cations (from monomers). Then chemical coupling of radical cations occurs. The most of the generated radical cations couple into short-chain oligomers and only a few fractions of them transfer into long-chain polymers, due to the extremely high oxidation ability of the MnO_4^-. The generated oligomers then dissolved into organic phase while the generated polymers are attached on the surface of the MnO_2 nuclei. Then, the high surface energy of the MnO_2 nuclei facilitates the anisotropic growth and the self-assembly process to reduce the surface energy. The coincidence of the anisotropic growth and the self-assembly process bring about the formation of submicron-sphere/nanosheet hierarchical structure. Importantly, the in situ generated PTh can act as structure directing agents to retard the agglomeration of MnO_2 nuclei, resulting in the generation of ultrathin nanosheets of MnO_2. The hydrophilic natures of the newly formed MnO_2 and polymers make the generated composite move away from the interface and then diffuse into the upper aqueous phase [46,47]. The morphology of the sample prepared by the co-precipitation route (with the absence of organic phase during synthesis) is shown in Fig. 4E and F. The two FESEM images clearly depict that agglomerated micron- or submicron-particles are generated by the co-precipitation route. The contrasting morphologies of the samples prepared by interfacial route and co-precipitation route highlight the advantage of the interfacial route to surpass the overgrowth of nuclei in nano-synthesis.

The electrochemical capacitive properties of the prepared nanocomposite were investigated by cyclic voltammetry (CV) and galvanostatic charge/discharge cycling. The CV plots of the electrode of PTh/MnO_2 nanocomposite, shown as the solid plots in Fig. 6A, display rectangular and enantiomorphous features, sug-

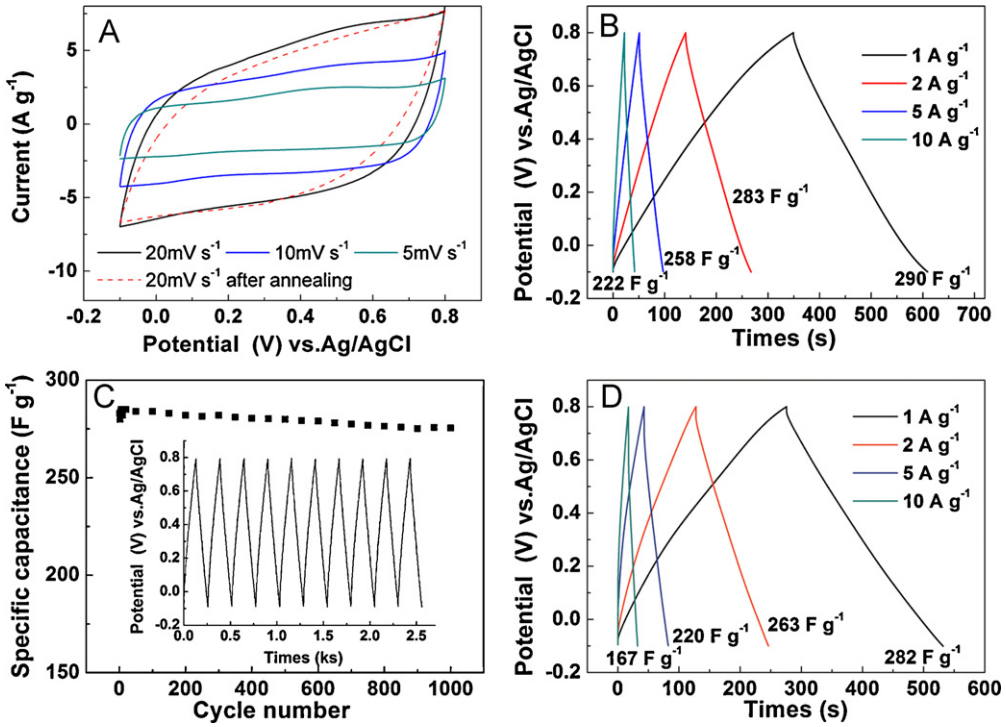

Fig. 6. (A) Cyclic voltammetric plots of the prepared nanocomposite electrode (solid curves) at different scan rates between −0.1 and 0.8 V in 1 M Na_2SO_4 solution. The dash line shows CV plot of the annealed nanocomposite electrode; (B) galvanostatic charge/discharge plots of the prepared nanocomposite electrode at different current densities; (C) cycle life of the prepared nanocomposite electrode derived from the galvanostatic charge/discharge cycling plots at 2 A g^{-1} (inset of C) and (D) galvanostatic charge/discharge plots of the annealed nanocomposite electrode. The mass loadings of the active materials for annealed and non-annealed electrodes are 1.38 and 1.47 mg cm^{-2}, respectively.

gesting good reversibility and ideal pseudocapacitive properties of the electrode. The ideal pseudocapacitive behaviors in a working potential window of 0.9 V indicate the contribution of MnO_2 is dominant in the nanocomposite. The domination of MnO_2 is benefit to enlarge the working potential window of the composite electrode since polymers generally have narrower working potential windows. The enlarged working potential window is probably derived from the interactions between polymers and birnessites since the interlayer gaps in the lattices of birnessites can accommodate the intercalations of polymers [40]. It is acknowledged that the exact interactions between polymers and birnessites still remain uncertain based on present results and the investigations are still ongoing. The specific capacitance values calculated from Fig. 6A are 273, 257 and 235 F g^{-1} at the scan rates of 5, 10 and 20 mV s^{-1}, respectively. The galvanostatic charge/discharge curves of the prepared nanocomposite electrode at different current densities are displayed in Fig. 6B. The specific capacitances estimated from Fig. 6B are found to be 290, 283, 258 and 222 F g^{-1} for the current densities of 1, 2, 5 and 10 A g^{-1}, respectively. At a high-rate charge/discharge process of 10 A g^{-1}, the nanocomposite electrode can still retain 76.6% of its capacitance at 1 A g^{-1}, suggesting its excellent high-power capability. The cycle performance of the nanocomposite electrode is investigated by galvanostatic charge/discharge cycles at 2 A g^{-1}, as presented in Fig. 6C. After a 1000-time cycle, the specific capacitance of the electrode remains at 275.5 F g^{-1}. The retention of 97.3% of its initial capacitance after 1000 cycles indicates the excellent cycle performance of the prepared nanocomposite electrode.

The above results show the prepared nanocomposite electrode has relatively large specific capacitance, good power capability and excellent cycle performance. The excellent electrochemical properties can be attributed to the unique microstructure and crystal structure of the nanocomposite.

Generally, manganese oxide electrodes can store charges via intercalation/extraction of proton or alkali cations into oxide lattices (reaction (1)) and surface adsorption/desorption of electrolyte cations (reaction (2)) [6,8–10].

$$MnO_2 + M^+ + e^- = MnOOM \quad (M^+ = Na^+, K^+ \text{ or } H_3O^+) \tag{1}$$

$$(MnO_2)_{surface} + M^+ + e^- = (MnO_2{}^-M^+)_{surface} \quad (M^+ = Na^+, K^+ \text{ or } H_3O^+) \tag{2}$$

The large specific surface area of the synthesized nanocomposite enlarges the contact area between active materials and electrolytes. This increased electrode/electrolyte interface area can facilitate the surface adsorption/desorption of protons or alkali cations (reaction (2)). Also, the crystal structure of the prepared birnessite-type MnO_2 nanocomposite contains an interlayer gap as large as 0.73 nm. The large interlayer gaps can accommodate different cations and then enhance the intercalation/extraction of protons or alkali cations into the lattices of birnessites (reaction (1)) [41,42]. Moreover, the mesoporous matrix of the prepared nanocomposite allows fast diffusion of electrolyte and ions. The enhanced diffusive efficiency contributes to the good high-power performance of the prepared nanocomposite electrode.

The important roles of the coated polymer were confirmed by the vastly different electrochemical properties of the annealed composite electrode and the non-annealed composite electrode. After annealing at 400 °C for 1 h, the electrode shows more distorted rectangular shape in CV plot, shown as a dash plot in Fig. 6A. The annealed composite electrode only conveys a specific capacitance of 195 F g^{-1}, while the non-annealed electrode gives a value of 235 F g^{-1}. The galvanostatic charge/discharge curves of the annealed electrode at different current densities are illustrated in Fig. 6D. The specific capacitances are 282, 263, 220 and 167 F g^{-1} for current densities of 1, 2, 5 and 10 A g^{-1}, respectively. At a high-rate galvanostatic charge/discharge process of 10 A g^{-1},

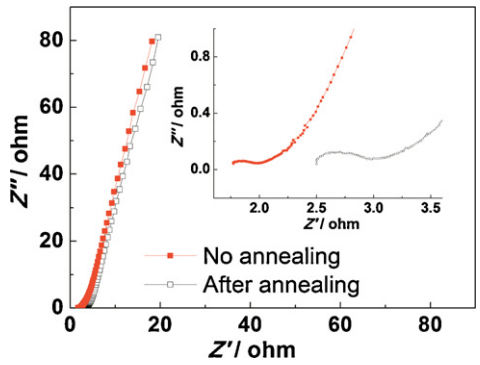

Fig. 7. Nyquist plots for the prepared nanocomposite electrode without (solid squares) and with (hollow squares) annealing at 400 °C for 1 h. The inset shows the plots in an enlarged scale.

the annealed electrode only remains 59.2% of its capacitance at 1 A g^{-1}. It is concluded that the high-rate electrochemical properties of MnO_2 are greatly enhanced by mixing PTh into birnessite nanosheets by comparing the electrochemical properties of both the annealed composite and non-annealed composite electrodes, although their low-rate electrochemical properties remain almost the same. The present PTh can not only enhance the electrical conductivity of the prepared composite electrode, but also acts as a stabilizer to stabilize the ultrathin nanosheets with high surface energy. The corresponding EIS plots displayed in Fig. 7 verify the lower electrical resistance of the PTh/MnO_2 electrode in comparison with the electrode without PTh (after annealing). As shown in Fig. 7, both Nyquist plots present depressed semi-circle over the high frequency range corresponding to the charge-transfer resistance and nearly straight sloped line in the low frequency region [5]. The nearly ideal straight sloped lines along the imaginary axis at the lower frequencies indicate the quasi-ideal capacitive behaviors for both electrodes. The equivalent series resistance (ESR) and the interfacial charge-transfer resistance (R_{ct}) can be deduced from the x intercept and the diameter of the semicircle of Nyquist plot, respectively. The ESR consists of the uncompensated electrical resistance of active materials, the resistance in electrolyte and the resistance of current collectors. The charge transfer resistance is originated from the electron transfer barrier between capacitive materials and the current collectors and also from the ion diffusion barrier between capacitive materials and electrolyte. Obviously, the PTh/MnO_2 electrode has relatively lower ESR and R_{ct} than those of the electrode without conducting polymers. The good conductivities of the conducting polymers in the PTh/MnO_2 composite electrode are believed to be beneficial to decrease ESR and R_{ct}. The decreased ESR and R_{ct} contribute to the enhanced pseudo-capacitive properties of the PTh/MnO_2 electrode. It is also acknowledged that the different R_{ct} values for two electrodes are also ascribed to their different ionic conductivities [41]. Heat-treatment can remove chemical-bonded hydrates from birnessite crystals. The removal of chemical-bonded hydrates causes the decreased ionic conductivity and thus the increased R_{ct} [48].

Another concern involving SCs is focused on the capacitance retention upon repeated cycling. The capacitance fading of the prepared nanocomposite electrodes is due to the following two reasons. The high surface energy of nanostructured materials tends to induce undesired side reactions with the electrolytes, although nanomaterials with large surface area can provide enhanced kinetics [11,12]. Manganese oxides with various valences can accommodate multiple redox reactions during charge/discharge processes. When MnO_2 is electro-reduced, some precursory solid MnO_2 is reduced to soluble species (such as Mn^{2+}). The soluble species can only be partially electro-recovered to solid MnO_2 through re-oxidation processes. The above dissolution–deposition processes cause the progressive loss of redox activities of electrodes. On the other hand, during charge/discharge processes, the expansion and shrinkage can occur in the lattices of manganese oxides [49,50]. The lattice changes derived from cations' insertion/extraction can induce volume changes in the active materials. The volume changes can cause the local stresses and the consequent failures of the electrodes [24]. The microstructure of the active electrode materials after cycles was studied by TEM to investigate the stability of the electrodes upon charge/discharge cycles. The prepared nanocomposite powders with or without annealing at 400 °C for 1 h were directly pressed on the porous nickel meshes with the same loading in order to eliminate the influences of binders and carbons. The both electrodes were then subjected to a consecutive 1000-time CV scan at a scan rate of 20 mV s^{-1} between −0.1 V and 0.8 V in 1 M Na_2SO_4 solution. After the electrochemical treatment, the powders collected from the forenamed electrodes were washed with deionised water and ethanol and then dried in air for TEM measurement. The corresponding TEM images are shown in Fig. 8. The PTh/MnO_2 powders largely retain their submicron-sphere/nanosheet hierarchical microstructure after CV scans, as displayed in Fig. 8A, suggesting the good stability of the prepared nanocomposite. The annealed powders lose their nanosheet features in morphology after the electrochemical treatment based on Fig. 8B, indicating the inferior stability of the intrinsic birnessite nanosheets. The contrasting morphology changes of the birnessite nanosheets with or without PTh compositing thus confirms that it is effective to stabilize the ultrathin birnessite nanosheets by compositing a fraction of PTh upon their surface. The enhanced

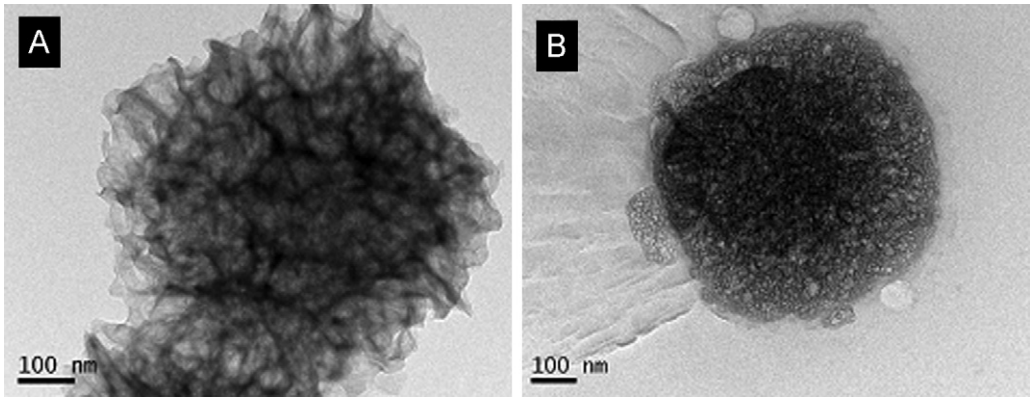

Fig. 8. Typical TEM images of the prepared nanocomposite without (A) or with (B) annealing at 400 °C for 1 h after a consecutive 1000-time CV scan at a scan rate of 20 mV s^{-1} between −0.1 and 0.8 V in 1 M Na_2SO_4 solution.

stability of the prepared PTh/MnO_2 nanocomposite guarantees the nanocomposite electrode to convey retention of 97.3% of its initial capacitance even after 1000 galvanostatic charge/discharge cycles at $2\,A\,g^{-1}$.

It is believed that this facile interfacial route is general and can be extended to other composite systems. The synthesized mesoporous PTh/MnO_2 nanocomposite with submicron-sphere/nanosheet hierarchical microstructure is also believed to be promising materials for batteries, electrocatalysts for oxygen reduction, sensors, etc.

4. Conclusions

In summary, mesoporous nanocomposite of polythiophene and MnO_2 with submicron-sphere/nanosheet hierarchical microstructure was synthesized by a facile one-pot interfacial method without the assistance of any templates, additional structure directing agents and complex precursors. It was demonstrated that this interfacial approach could effectively suppress overgrowth of the nuclei and lead to the formation of polythiophene/MnO_2 nanosheets with a diameter less than 10 nm. At a high-rate charge/discharge process of $10\,A\,g^{-1}$, the nanocomposite electrode can still retain 76.6% of its capacitance at $1\,A\,g^{-1}$. The retention of 97.3% of its initial capacitance after 1000 cycles at a charge/discharge rate of $2\,A\,g^{-1}$ indicates the excellent cycle performance of the prepared nanocomposite electrode. The enhanced electrochemical-capacitive properties of the polythiophene/MnO_2 nanocomposite electrode were rationalized to its unique microstructure. In particular, the in situ generated polythiophene was proven to be effective not only on increasing the electrical conductivity but also on improving the electrochemical stability of the nanocomposite electrode. This finding enlarges our understanding of conducting polymer/oxide composites and provides us a hint to develop high-effective electrode materials for advanced electrochemical energy storage/conversion systems.

Acknowledgements

We acknowledge the financial supports from National Basic Research Program of China (973 Program, No. 2009CB320301) and National Natural Science Foundation of China (30901198).

References

[1] P. Simon, Y. Gogotsi, Nat. Mater. 7 (2008) 845–854.
[2] J.R. Miller, A.F. Burke, Electrochem. Soc. Interface 17 (2008) 53–57.
[3] C.C. Hu, C.C. Wang, Electrochem. Commun. 4 (2002) 554–559.
[4] C.C. Hu, T.W. Tsou, Electrochem. Commun. 4 (2002) 105–109.
[5] W. Xiao, H. Xia, J.Y.H. Fuh, L. Lu, J. Electrochem. Soc. 156 (2009) A627–A633.
[6] W. Xiao, H. Xia, J.Y.H. Fuh, L. Lu, J. Power Sources 193 (2009) 935–938.
[7] D. Belanger, T. Brousse, J.W. Long, Electrochem. Soc. Interface 17 (2008) 49–52.
[8] H.Y. Lee, J.B. Goodenough, J. Solid State Chem. 144 (1999) 220–223.
[9] S.C. Pang, M.A. Anderson, T.W. Chapman, J. Electrochem. Soc. 147 (2000) 444–450.
[10] S.F. Chin, S.C. Pang, M.A. Anderson, J. Electrochem. Soc. 149 (2002) A379–A384.
[11] Y.G. Guo, J.S. Hu, L.J. Wan, Adv. Mater. 20 (2008) 2878–2887.
[12] A.S. Arico, P. Bruce, B. Scrosati, J.M. Tarascon, W. van Schalkwijk, Nat. Mater. 4 (2005) 366–377.
[13] X. Wang, Y.D. Li, Chem. Eur. J. 9 (2003) 300–306.
[14] H.T. Zhu, J. Luo, H.X. Yang, J.K. Liang, G.H. Rao, J.B. Li, Z.M. Du, J. Phys. Chem. C 112 (2008) 17089–17094.
[15] J. Luo, H.T. Zhu, H.M. Fan, J.K. Liang, H.L. Shi, G.H. Rao, J.B. Li, Z.M. Du, Z.X. Shen, J. Phys. Chem. C 112 (2008) 12594–12598.
[16] J. Jamnik, R. Dominko, B. Erjavec, M. Remskar, A. Pintar, M. Gaberscek, Adv. Mater. 21 (2009) 2715–2719.
[17] R.N. Reddy, R.G. Reddy, J. Power Sources 124 (2003) 330–337.
[18] J.Y. Luo, Y.Y. Xia, J. Electrochem. Soc. 154 (2007) A987–A992.
[19] A.E. Fischer, M.P. Saunders, K.A. Pettigrew, D.R. Rolison, J.W. Long, J. Electrochem. Soc. 155 (2008) A246–A252.
[20] H.Y. Lee, S.W. Kim, H.Y. Lee, Electrochem. Solid State Lett. 4 (2001) A19–A22.
[21] Y.T. Wu, C.C. Hu, J. Electrochem. Soc. 151 (2004) A2060–A2066.
[22] X. Zhang, L. Ji, S. Zhang, W. Yang, J. Power Sources 173 (2007) 1017–1023.
[23] X. Jin, W. Zhou, S. Zhang, G.Z. Chen, Small 3 (2007) 1513–1517.
[24] R. Liu, S.B. Lee, J. Am. Chem. Soc. 130 (2008) 2942–2943.
[25] A.V. Murugan, J. Power Sources 159 (2006) 312–318.
[26] E.C. Rios, A.V. Rosario, R.M.Q. Mello, L. Micaroni, J. Power Sources 163 (2007) 1137–1142.
[27] S.R. Sivakkumar, J.M. Ko, D.Y. Kim, B.C. Kim, G.G. Wallace, Electrochim. Acta 52 (2007) 7377–7385.
[28] M.Q. Wu, G.A. Snook, G.Z. Chen, D.J. Fray, Electrochem. Commun. 6 (2004) 499–504.
[29] X. Zhang, W.S. Yang, Y.W. Ma, Electrochem. Solid State Lett. 12 (2009) A95–A98.
[30] K. Naoi, M. Morita, Electrochem. Soc. Interface 17 (2008) 44–48.
[31] G.A. Snook, C. Peng, D.J. Fray, G.Z. Chen, Electrochem. Commun. 9 (2007) 83–88.
[32] C. Peng, J. Jin, G.Z. Chen, Electrochim. Acta 53 (2007) 525–537.
[33] L. Chen, X.G. Zhang, C.Z. Yuan, S.Y. Chen, Acta Phys.-Chim. Sin. 25 (2009) 304–308.
[34] X.H. Yang, Y.G. Wang, H.M. Xiong, Y.Y. Xia, Electrochim. Acta 53 (2007) 752–757.
[35] C. Yuan, B. Gao, L. Su, X. Zhang, J. Colloid Interface Sci. 322 (2008) 545–550.
[36] N. Masaharu, K. Yoshinori, S. Kazushi, J. Electrochem. Soc. 156 (2009) D125–D130.
[37] F.J. Liu, J. Power Sources 182 (2008) 383–388.
[38] W.M. Zhang, X.L. Wu, J.S. Hu, Y.G. Guo, L.J. Wan, Adv. Funct. Mater. 18 (2008) 3941–3946.
[39] Y.G. Wang, Y.R. Wang, E. Hosono, K.X. Wang, H.S. Zhou, Angew. Chem. Int. Ed. 47 (2008) 7461–7465.
[40] Y.G. Wang, W. Wu, L. Cheng, P. He, C.X. Wang, Y.Y. Xia, Adv. Mater. 20 (2008) 2166–2170.
[41] O. Ghodbane, J.L. Pascal, F.D.R. Favier, ACS Appl. Mater. Interfaces 1 (2009) 1130–1139.
[42] S. Devaraj, N. Munichandraiah, J. Phys. Chem. C 112 (2008) 4406–4417.
[43] H.M. Wang, G.Q. Tang, S.S. Jin, C.X. Bian, F.F. Han, D. Liang, X.C. Xu, Acta Chim. Sin. 65 (2007) 2454–2458.
[44] X.G. Li, J. Li, M.R. Huang, Chem. Eur. J. 15 (2009) 6446–6455.
[45] Y. Omomo, T. Sasaki, M. Watanabe, Solid State Ionics 151 (2002) 243–250.
[46] J.K. Yuan, K. Laubernds, Q.H. Zhang, S.L. Suib, J. Am. Chem. Soc. 125 (2003) 4966–4967.
[47] N. Nurxat, K. Su, N.I. Yang, H. Matsui, ACS Nano 2 (2008) 502–506.
[48] K. Rajendra Prasad, N. Miura, Electrochem. Commun. 6 (2004) 1004–1008.
[49] S.L. Kuo, N.L. Wu, J. Electrochem. Soc. 153 (2006) A1317–A1324.
[50] L. Athouel, F. Moser, R. Dugas, O. Crosnier, D. Belanger, T. Brousse, J. Phys. Chem. C 112 (2008) 7270–7277.